

Effective Permittivity Measurement of 3D-Printed Dielectric Crystals

Simon P. Hehenberger*, Aparna P. T. Adithyababu *, Stefano Caizzone*,

*Institute of Communication and Navigation, German Aerospace Center (DLR), Wessling, Germany,

Contact email: simon.hehenberger@dlr.de

Abstract—Additive manufacturing offers new possibilities in innovative antennas and microwave components. In order to fully exploit its potential, it is necessary to exploit the capabilities offered by the 3D printing technology fully. 3D-printed structured dielectrics are currently receiving much interest in this respect. However, the characterization of the dielectric properties of such crystal structures is not easy, and assumptions on such properties need to be made often. This paper shows a characterization of additively manufactured structured dielectrics in terms of their permittivity and loss tangent in a simple cubic (SC) and face-centered cubic (FCC) crystal geometry with different fill fractions. Measurement results are compared to values predicted by the Maxwell-Garnett effective media approximation and the effective refractive index extracted from a three-dimensional plane wave expansion method (PWEM) in the long-wavelength limit.

Index Terms—structured dielectrics, dielectric crystals, 3D-printing, material parameter estimation, material parameter measurement, effective permittivity, pwem, maxwell-garnett

I. INTRODUCTION

Printed circuit boards dominate the current state of the art in microwave component manufacturing combined with chemical etching or precise milling processes. Although these processes allow the manufacturing of very tight tolerances, they come with their own sets of problems and are usually time-consuming and expensive to manufacture. In the last decade, the possibilities enabled by additive manufacturing (AM) exploded, and researchers increasingly try incorporating the additional degrees of freedom offered by AM to design and manufacture new microwave components [1]. Devices based on metalizing 3D printed structures have been of some interest but ultimately defy the leading 3D printing argument of being cheap and ready out of the machine due to the often cumbersome and expensive metallization [2]. Moving away from metals, devices such as dielectric resonator antennas [3][4], lenses [5] and substrates [6] have been designed and printed as solids and also with graded-index approaches, where different fill-fractions of some base material are used to create inhomogeneous structures. However, the works mentioned above only employ a quasi 3D approach, utilizing rectangular, triangular, or hexagonal infill grids periodic in two dimensions and provided by a 3D slicer software to spatially modulate the dielectric permittivity. Although yielding good results, this approach lacks design freedom since the infill grids are relatively simple, and the third dimension is not exploited fully in the design. A more promising approach is to come up with

parametrically defined unit cells arranged in a 3D grid which offers the benefit of 3D spatial control of the permittivity, as reported in [7]. An excellent example of this approach is done in [8] by 3D printing a multi-permittivity dielectric resonator antenna (DRA) with a high permittivity base material on a 3D grid. However, the resin and printer utilized in [8] are pretty expensive, and no insight into the unit-cell design is given. This paper utilizes a more general approach by employing spatial harmonics for unit-cell definition in any crystal geometry. Several sample lattices with SC and FCC geometry are manufactured employing additive manufacturing and characterized in their effective permittivity and loss tangent. They are allowing to explore the additive manufacturing of dielectric crystal lattices with low-cost fused deposition modeling printers. The paper is structured as follows. First, dielectric crystals' design via spatial harmonics thresholding is described. Second, effective permittivity computation is introduced via the Maxwell-Garnett (MGA) effective media approximations and a 3D plane wave expansion method (PWEM). The third section gives a short overview of the tradeoffs involved in dielectric material characterization and describes the utilized measurement system. Furthermore, section three details the results obtained from Rogers substrate samples used for validating the measurement system. In the last section, the additively manufactured samples are explained in detail, and measurement results are discussed and compared to predictions from MGA and PWEM simulations.

II. DIELECTRIC CRYSTALS

In contrast to other works where unit cells are parametrically defined [6][9], this work takes a different approach and defines unit-cells via spatial harmonics along the reciprocal lattice vectors of the desired crystal geometry.

A. Simple cubic and face centered cubic Bravais lattices

Considering SC and FCC Bravais lattices in the cubic crystal structure, which are defined by their lattice constant a and their respective primitive lattice vectors \vec{t}_1 , \vec{t}_2 and \vec{t}_3 which point from the current lattice node to its three nearest neighbors, as depicted in Figure 1. For each set of two primitive lattice

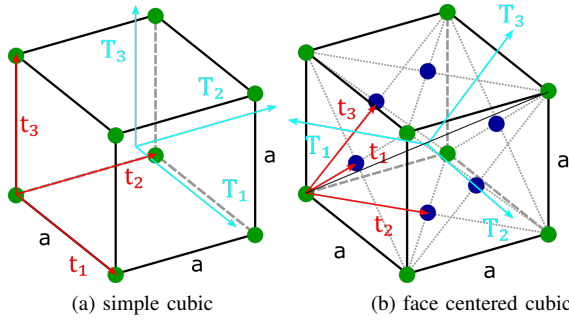


Fig. 1. Geometries of (a) simple cubic and (b) face centered cubic with lattice constant a , primitive lattice vectors \vec{t}_1 , \vec{t}_2 and \vec{t}_3 and reciprocal lattice vectors \vec{T}_1 , \vec{T}_2 and \vec{T}_3 .

vectors, a perpendicular reciprocal lattice vector vector, can be found via

$$\vec{T}_1 = 2\pi \frac{\vec{t}_2 \times \vec{t}_3}{\vec{t}_1 \cdot (\vec{t}_2 \times \vec{t}_3)} \quad (1)$$

$$\vec{T}_2 = 2\pi \frac{\vec{t}_3 \times \vec{t}_1}{\vec{t}_2 \cdot (\vec{t}_3 \times \vec{t}_1)} \quad (2)$$

$$\vec{T}_3 = 2\pi \frac{\vec{t}_1 \times \vec{t}_2}{\vec{t}_3 \cdot (\vec{t}_1 \times \vec{t}_2)} \quad (3)$$

where the magnitude describes the periodicity of the lattice.

B. Lattice generation via spatial harmonics

The lattice geometry in the respective Bravais lattice is now created by calculating a superposition of N spatial harmonics with individual grating vectors \vec{g}_i , $i = 1 \dots N$,

$$A = \sum_{i=1}^N A_i e^{j(g_i x + g_i y + g_i z)} \quad (4)$$

where the complex weights of individual harmonics A_i are normalized such that A is a complex valued function in terms of spatial coordinates x , y and z with magnitude between 0 and 1.

By choosing the individual grating vectors \vec{g}_i such that they are oriented along the reciprocal lattice vectors \vec{T}_i as defined in (3) and their periodicity is an integer multiple of the lattice periodicity, the superposition of spatial harmonics will obtain the respective crystal symmetry and periodicity. The overall lattice L is computed, for some threshold $th \in [0, 1]$, on the min-max feature scaled real part of the superimposed spatial harmonics A

$$L := \frac{Re\{A\} - \min(Re\{A\})}{\max(Re\{A\}) - \min(Re\{A\})} \geq th. \quad (5)$$

The resulting geometry is converted into a standard tessellation (STL) file that can be interpreted by 3D printing slicer software, which generates the necessary G-code for the respective additive manufacturing machine.

Figure 2 shows individual unit cells in SC and FCC created with $N = 3$ spatial harmonics, with grating vectors equal to the reciprocal lattice vectors ($\vec{g}_i = \vec{T}_i$), as explained above

and with different thresholds $th \in \{0.2, 0.4, 0.6, 0.8\}$. The reason for utilizing spatial harmonics to create the unit cell geometry is that one can easily vary the fill fraction by changing the threshold value throughout the lattice or even within one unit cell. Therefore, providing better resolution for index graded devices than unit cells that are parametrically defined. Furthermore, any unit cell geometry in any crystal system can be decomposed and represented by a discrete set of spatial harmonics with complex weights. This bears the benefit that the described approach is much more general and effective for handling 3D lattices. Furthermore, the utilization of spatial harmonics to represent periodic structures makes the applications of algorithms to spatially vary the lattice, as proposed in [10], more accessible and computationally efficient.

III. SIMULATION OF EFFECTIVE MATERIAL PARAMETERS

In the following, the MGA and PWEM are briefly introduced in this section. However, actual results from the methods are only presented in comparison to measurements in section V.

A. Maxwell-Garnett effective media approximation

The effective dielectric permittivity ε_{eff} of some material composed of some dielectric ε_m and filled with dielectric spheres with permittivity ε_i can be estimated with the Maxwell-Garnett approximation

$$\frac{\varepsilon_{eff} - \varepsilon_m}{(\varepsilon_{eff} + 2\varepsilon_m)} = \delta_i \frac{\varepsilon_i - \varepsilon_m}{(\varepsilon_i + 2\varepsilon_m)} \quad (6)$$

where δ_i is the volume fill fraction of the inclusions. Although it has been reported that the MGA does not deliver good results for larger fill-fractions [11], it has been used with success to predict permittivities of index graded devices [12]. For known dielectric permittivities and fill fractions the effective permittivity of a lattice L is easily found.

B. Plane Wave Expansion Method (long-wavelength limit)

The PWEM is an efficient Fourier space technique to solve the Maxwell's equations in inhomogeneous or periodic media with low to moderate dielectric contrast as an eigenvalue problem. Based on the description of some infinitely periodic unit cell, and a given Bloch vector $\vec{\beta}$, the PWEM computes the modes (eigenvectors) that fit the phase boundary condition imposed by the selected Bloch vector $\vec{\beta}$ and their respective wavenumbers k_0 (eigenvalues). For Bloch vector $\vec{\beta}$ magnitudes much smaller than the lattice constant ($|\vec{\beta}| \ll a$, long-wavelength limit), the ratio between the Bloch vector magnitude and the respective wavenumber can be used to predict the effective refractive index

$$n_{eff} = \sqrt{\varepsilon_r \mu_r} = \frac{|\vec{\beta}|}{k_0}, \quad (7)$$

which for purely dielectric media ($\mu_r = 1$), is the square root of the effective permittivity. The PWEM is an efficient tool for computing modes in periodic dielectric structures.

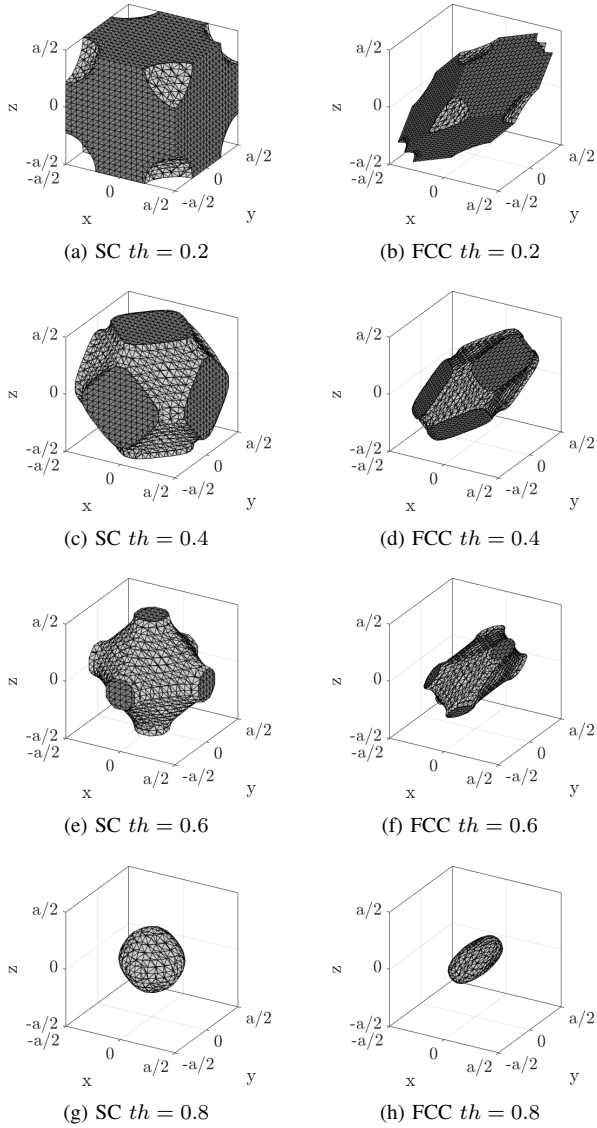


Fig. 2. Unit-cells created by thresholding superimposed spatial harmonics in the direction of the reciprocal lattice vectors of the respective SC and FCC crystal geometries. The faces touching the boundaries of the crystal unit cell are shaded darker than faces which do not.

However, being a Fourier space method, it suffers from the Gibbs phenomenon, which is particularly problematic when considering structures with high index contrast. Furthermore, attention has to be paid to the convergence of the method.

IV. MEASUREMENT SYSTEM

The characterization of dielectric materials is rather difficult, and several different methods have been developed to deal with this topic in theory, simulation, and experiments. If a given measurement technique is suitable to estimate permittivity and loss tangent of some sample depends on a large number of factors, for example frequency of interest (broadband or resonant), expected permittivity and loss-tangent range, required accuracy, sample material composition (solid, liquid, powdered, etc.), sample shape, size and machinability and



Fig. 3. System to measure dielectric permittivity consisting of an aluminium ground plate, feeder printed circuit board (PCB) with a Microstrip line, a resonator PCB with a Microstrip ring resonator and 3D printed support glued to its back and a sample of 3D printed lattice structure in FCC geometry.

many others [13]. The measurement setup in this work relies on a resonant method, a suspended Microstrip ring resonator introduced in [14] and depicted in Figure 3, to characterize 3D printed lattices in terms of their permittivity and dielectric loss. The main components of the suspended Microstrip ring resonator measurement system are a feeder printed circuit board (PCB) and a resonator PCB, where the former is placed below the latter. The resonator PCB has a Microstrip ring resonator on its bottom surface, and a rectangular strip of polylactic acid (PLA) glued to the upper surface. The PLA provides extra support to the resonator PCB and prevents bending or deforming due to the suspended position or pressure from a sample. During a measurement, the sample is placed between feeder and resonator PCB, and an S-parameter measurement is performed, with and without the sample under test and the difference in the first resonance frequency $\Delta f = f_{res2} - f_{res1}$ and bandwidth $\Delta B = B_2 - B_1$ is extracted. Figure 4 depicts the measured S_{12} parameter with and without a Rogers 5870 sample and denotes the difference in resonance frequency and bandwidth. Estimating the dielectric permittivity and loss tangent is later performed with Δf and ΔB using polynomials extracted from CST simulations. Before utilizing the measurement setup to characterize 3D printed samples, it has been verified by using different Rogers substrates with permittivity $\epsilon_{r,ref}$ found in their respective datasheets as reference. The results of this verification are presented in Table I and fit the reference permittivities and loss tangents from the datasheets well. Although the results of the validation in Table I fit the expected values well, it has to be emphasized that the capabilities of the described measurement system are not suited to characterize samples fully. Due to the measurement system's resonant nature, the extracted permittivity and loss tangent are only valid at the resonant frequency point, providing no insight into the material properties broadband behavior.

V. CHARACTERIZATION OF 3D PRINTED SAMPLES

For the measurements of 3D printed samples, SC and FCC lattices with $N = 3$ spatial harmonics, with grating vectors equal to the individual spatial reciprocal lattice vectors of the respective lattices, are used to create the samples. In order to test the predictions about the effective dielectric

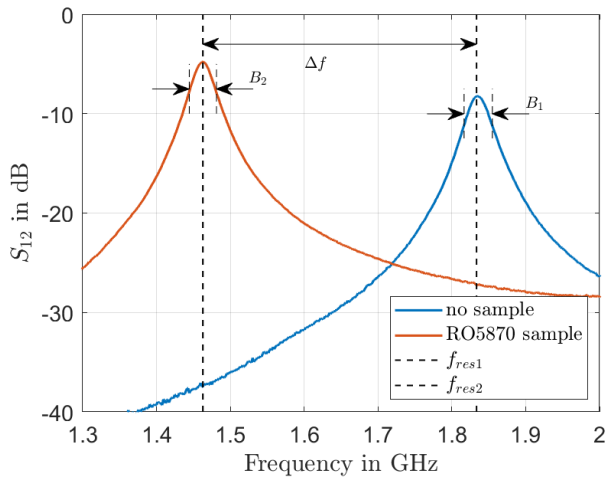


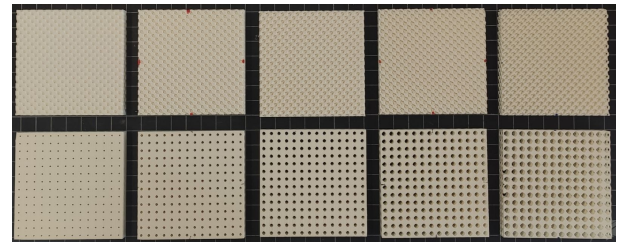
Fig. 4. Measured S_{12} parameters of a suspended Microstrip measurement system with and without a Rogers 5870 substrate sample.

TABLE I

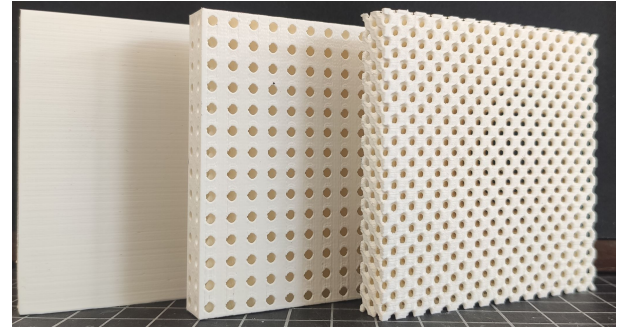
CHARACTERIZATION OF DIFFERENT ROGERS MATERIALS IN TERMS OF DIELECTRIC PERMITTIVITY AND LOSS TANGENT FOR VERIFICATION OF THE SUSPENDED MICROSTRIP MEASUREMENT SETUP. REFERENCE VALUES TAKEN FROM THE RESPECTIVE ROGERS MATERIALS DATASHEETS.

Material	$\epsilon_{r,ref}$	$\tan\delta_{ref}$	$\epsilon_{r,meas}$	$\tan\delta_{meas}$
RO5870	2.33 ± 0.02	0.0012	2.28	0.0007
RO4003C	3.38 ± 0.05	0.0027	3.34	0.0016
RO6006	6.15 ± 0.15	0.0027	5.74	0.0024
RO6010	10.2 ± 0.25	0.0023	10.31	0.0021

permittivity obtained from of MGA theory and PWEM simulation, multiple lattices in SC and FCC with thresholds $th \in \{0.35, 0.4125, 0.475, 0.5375, 0.6\}$ were manufactured with a lattice constant of $a = 5$ mm in a cubic volume of $70 \times 70 \times 10$ mm³. The individual lattices were printed with an Ultimaker 3 using white polylactide (PLA) filament from Ultimaker at a temperature of 200°C and 150-micrometer layer height. Figure 5a depicts all the samples that were printed for characterization. Furthermore, a more detailed picture of the bulk, SC, and FCC sample in comparison is provided in Figure 5b. In addition, a bulk sample with the same volumetric dimensions and 100 percent infill was printed to measure the permittivity and loss tangent of the PLA base material. The measured results for the individual samples are listed in Table II as well as plotted together with simulation results as a function of th in Figure 6a and 6b for SC and FCC samples respectively. For both SC and FCC samples, we see that predictions by MGA theory and PWEM simulations do not differ much and predict the effective relative dielectric permittivity of the crystal lattices very well. However, the results are lacking in terms of broadband characterization due to the resonant nature of the measurement system. Due to the periodic nature of the samples, they will naturally exhibit an upper cutoff frequency at which the assumption of a lattice constant much smaller than the applied wavelength is not valid anymore. The currently employed measurement approach



(a) all



(b) detail

Fig. 5. Additively manufactured dielectric crystal structures with SC and FCC lattice geometries. (a) all manufactured samples. (b) samples in detail, BULK, SC, FCC (from left to right).

TABLE II

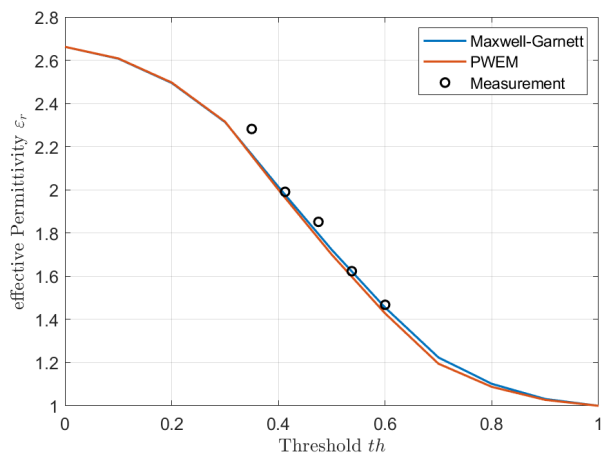
CHARACTERIZATION OF ADDITIVELY MANUFACTURED DIELECTRIC CRYSTALS WITH SIMPLE CUBIC (SC) AND FACE CENTERED CUBIC (FCC) GEOMETRIES IN TERMS OF THEIR DIELECTRIC PERMITTIVITY AND LOSS TANGENT.

Sample		MGA	PWEM	Measurement	
Crystal	th	ϵ_r	ϵ_r	ϵ_r	$\tan\delta$
BULK	-	-	-	2.66	0.062
SC	0.35	2.17	2.17	2.28	0.044
SC	0.4125	1.98	1.96	1.99	0.042
SC	0.475	1.79	1.77	1.85	0.037
SC	0.5375	1.62	1.60	1.62	0.031
SC	0.6	1.45	1.43	1.47	0.025
FCC	0.35	2.17	2.14	2.27	0.043
FCC	0.4125	1.98	1.93	1.88	0.04
FCC	0.475	1.79	1.75	1.76	0.038
FCC	0.5375	1.62	1.56	1.5	0.029
FCC	0.6	1.45	1.4	1.39	0.024

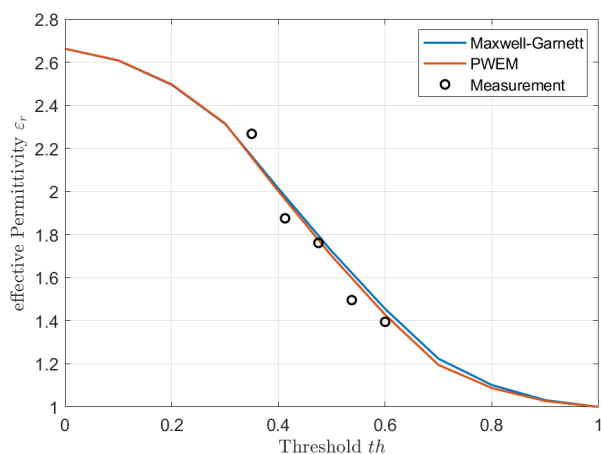
cannot determine this upper cutoff frequency.

VI. CONCLUSION

A method to create dielectric crystal lattices in arbitrary crystal geometries based on spatial harmonics along the reciprocal lattice vectors has been presented and successfully used to manufacture said lattices in SC and FCC Bravais lattices additively. Two simulation techniques, namely the Maxwell-Garnett theory and the plane wave expansion method, have been discussed to predict the effective dielectric permittivity of dielectric crystal lattices with different fill fractions. A measurement system for dielectric permittivity measurements



(a) simple cubic



(b) face centered cubic

Fig. 6. Comparison of effective dielectric permittivity of dielectric crystal lattices in (a) simple cubic and (b) face centered cubic geometries as a function of the threshold th used to sweep the fill-fraction of said lattices.

based on a suspended microstrip ring resonator was explained, and the results from system verification measurements have been presented. Simulations and measurements of effective permittivity and loss tangent of manufactured dielectric crystal lattices are discussed and agree with the prediction from theoretical effective material approximations.

REFERENCES

- [1] E. Rosker, R. Sandhu, J. Hester, M. Goorsky, and J. Tice, *Printable Materials for the Realization of High Performance RF Components: Challenges and Opportunities*, Int. J. Antennas Propag. 2018, 1–19 (2018).
- [2] K. Lomakin et al., *3D Printed Slotted Rectangular Hollow Waveguides*, 2019 IEEE MTT-S International Microwave Symposium (IMS), 2019, pp. 342-345, doi: 10.1109/MWSYM.2019.8700864.
- [3] A. A. Althwayb et al., *3-D-Printed Dielectric Resonator Antenna Arrays Based on Standing-Wave Feeding Approach*, in IEEE Antennas and Wireless Propagation Letters, vol. 18, no. 10, pp. 2180-2183, Oct. 2019, doi: 10.1109/LAWP.2019.2939734.
- [4] Z. -X. Xia, K. W. Leung and K. Lu, *3-D-Printed Wideband Multi-Ring Dielectric Resonator Antenna*, in IEEE Antennas and Wireless Propagation Letters, vol. 18, no. 10, pp. 2110-2114, Oct. 2019, doi: 10.1109/LAWP.2019.2938009.

- [5] J. W. Allen and B.-I. Wu *Design and fabrication of an RF GRIN lens using 3D printing technology*, Proc. SPIE 8624, Terahertz, RF, Millimeter, and Submillimeter-Wave Technology and Applications VI, 86240V (27 March 2013); <https://doi.org/10.1117/12.2000708>
- [6] Zhang, S., Njoku, C.C., Whittow, W.G. and Vardaxoglou, J.C. (2015), *Novel 3D printed synthetic dielectric substrates*, Microw. Opt. Technol. Lett., 57: 2344-2346. <https://doi.org/10.1002/mop.29324>
- [7] Tribe, J., Whittow, W., Kay, R. and Vardaxoglou, J. (2014), *Additively manufactured heterogeneous substrates for three-dimensional control of local permittivity*, Electron. Lett., 50: 745-746. <https://doi.org/10.1049/el.2014.1174>
- [8] Q. Lamotte et al., *Multi-permittivity 3D-printed Ceramic Dual-Band Circularly Polarized Dielectric Resonator Antenna for Space Applications*, 2021 15th European Conference on Antennas and Propagation (EuCAP), 2021, pp. 1-5, doi: 10.23919/EuCAP51087.2021.9411245.
- [9] Morales, C.D., Morlaas, C., Chabory, A., Pascaud, R., Grzeskowiak, M. and Mazingue, G. (2021), *3D-printed ceramics with engineered anisotropy for dielectric resonator antenna applications*, Electron. Lett., 57: 679-681. <https://doi.org/10.1049/el12.12234>
- [10] Raymond C. Rumpf and Javier Pazos, *Synthesis of spatially variant lattices,* Opt. Express 20, 15263-15274 (2012)
- [11] Mishchenko MI, Dlugach JM, Liu L. *Applicability of the effective-medium approximation to heterogeneous aerosol particles*, J Quant Spectrosc Radiat Transf 2016;178:284–94.
- [12] A. Goulas, S. Zhang, J.R. McGhee, D.A. Cadman, W.G. Whittow, J.C. Vardaxoglou, D.S. Engström. *Fused filament fabrication of functionally graded polymer composites with variable relative permittivity for microwave devices*, Mater. Des., 193 (2020), p. 108871, 10.1016/j.matdes.2020.108871
- [13] Clarke, R.N., Gregory, A.P., Cannell, D.S., Patrick, M.L., Wylie, S.J., Youngs, I.J., & Hill, G.J. (2003). *A guide to the characterisation of dielectric materials at RF and microwave frequencies*.
- [14] Waldron I, *Ring Resonator Method for Dielectric Permittivity Measurements of Foams*, Scott Biederman Thesis Comm Gen Mot. 2006;65.